

Unsupervised Learning on Monocular Videos for 3D Human Pose Estimation

Sina Honari^{1*}, Victor Constantin¹, Helge Rhodin², Mathieu Salzmann¹, Pascal Fua¹

¹CVLab, EPFL, Lausanne, Switzerland

²Imager Lab, UBC, Vancouver, Canada

Abstract

In this paper, we introduce an unsupervised feature extraction method that exploits contrastive self-supervised (CSS) learning to extract rich latent vectors from single-view videos. Instead of simply treating the latent features of nearby frames as positive pairs and those of temporally-distant ones as negative pairs as in other CSS approaches, we explicitly separate each latent vector into a time-variant component and a time-invariant one. We then show that applying CSS only to the time-variant features, while also reconstructing the input and encouraging a gradual transition between nearby and away features yields a rich latent space, well-suited for human pose estimation. Our approach outperforms other unsupervised single-view methods and match the performance of multi-view techniques.

1. Introduction

While supervised body pose estimation is rapidly becoming a mature field, the bottleneck remains the availability of sufficiently large training datasets, which cannot be guaranteed for many kinds of human motions. An effective way to address this is to leverage unsupervised data to learn a low-dimensional representation of poses. Then, it only takes very little annotated data to train a regressor to predict 3D poses from this representation. Key to the success of this approach is a good unsupervised learning objective, for which many existing techniques exploit the availability of multi-view footage [17, 24, 28, 20, 18]. However, recording with multiple synchronized cameras is strenuous and more demanding.

In this paper, we introduce an alternative unsupervised representation learning strategy for human pose estimation using videos acquired by a *single* RGB camera. To this end, we build on the idea of contrastive self-supervised (CSS) learning [16, 9, 3]. For any given sample, CSS aims to maximize the similarity to a positive sample and the dissimilarity to a negative one. In our context, one way to do

so is to treat a video frame close to the one of interest as positive sample, and a temporally-distant one as negative sample [1, 21]. We will show, however, that this strategy is insufficient while decoding image because it does not account for the fact that, when someone moves, some information, such as garment appearance, remains constant over time, while other information, such as the person’s pose, changes.

To overcome this, we therefore introduce a representation learning strategy that explicitly separates each latent vector into a *time-variant* component and a *time-invariant* one. We then exploit CSS learning to model the intuition that the time-changing component evolves smoothly, and thus the time-changing components of two poses that are close in time should, in general, be more similar compared to those of poses that are temporally distant. Fig. 1 summarizes our approach.

It differs from typical CSS strategies in two ways: First, we encourage a gradual transition from temporally close to temporally distant frames by applying the a novel contrastive formulation only to the time-changing components. Second, we explicitly perform image re-synthesis by mapping the latent vectors back to the images. When observing subjects in free fall, such as divers, we complement our CSS formalism with a prior encoding gravity to help the model detect the subject. Our experiments demonstrate that these three components help the model learn in an unsupervised manner a rich, low-dimensional latent representation of human motions from ordinary video sequences acquired using standard monocular RGB cameras.

Given this representation, a mapping to 3D pose can be learned from a very limited amount of annotated data. We demonstrate the benefits of our approach for pose estimation on three real-world RGB datasets. We show that it outperforms other unsupervised monocular approaches and yields results on par with unsupervised multi-view setups, while being much easier to deploy. In particular, it can exploit both monocular and multi-view videos when available, which a purely multi-view setup cannot. We will make our code publicly available.

*sina.honari@epfl.ch

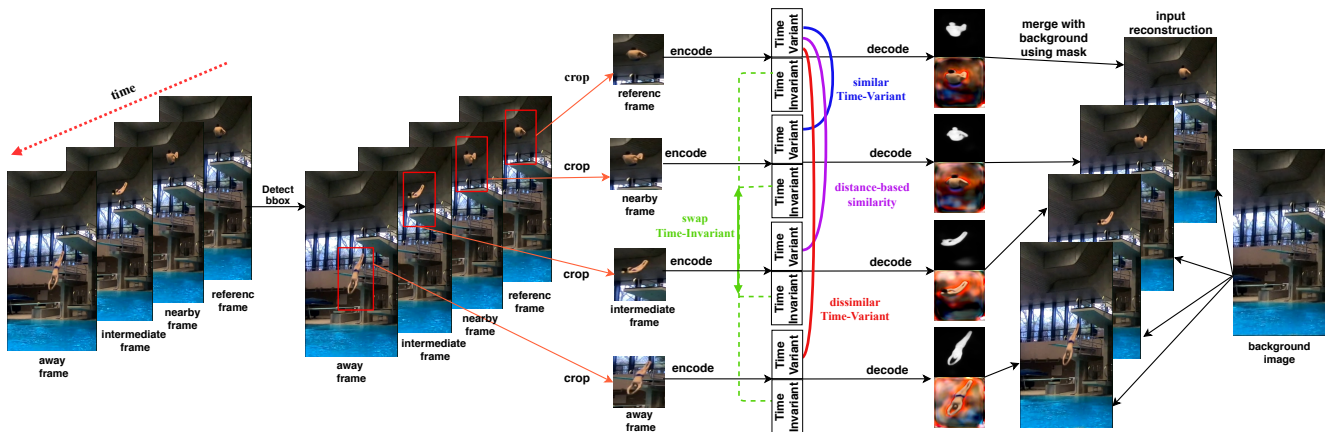


Figure 1. **Approach.** Given a reference frame, we sample a temporally close, far, and intermediate—between close and far—frame. The model first detects the person in all frames using a spatial transformer network. The detected regions are then cropped and encoded into *time-variant* and *time-invariant* components. The time-variant of the reference frame is made similar to that of the nearby frame and dissimilar to that of the away frame, while a distance-dependent similarity or dissimilarity is enforced between the reference and intermediate frames. To promote invariance of the time-invariant components, that of the reference and nearby frames are randomly swapped with the intermediate or away frames. The model then decodes each frame into a segmentation mask and an image. The decoded image is then merged with the background using the bounding box location and the decoded mask. No annotations are used (neither for detection, nor for segmentation) and the same network weights are used for all frames. At test time, the model can process a single frame.

2. Related Work

Unsupervised and self-supervised learning [2, 5] techniques have received considerable attention in recent years as a means to decrease the amount of training data required to train deep networks. We briefly review some of the methods most closely related to our work.

Single-View Approaches. Unsupervised learning for general video processing has been extensively researched. For example, LSTMs have been used to learn representations of video sequences [22]. Similarly, optical-flow and color diversity across frames has been leveraged to learn latent features corresponding to motion and appearance [25]. Multiple papers [14, 12, 6, 27] use the temporal order of frames to learn latent features from videos. In particular, the models of [14, 6] classify whether a set of frames have correct ordering or not, whereas those of [12, 27] predict the order of the frames or clips as a classification task. In [26], instead of relying on temporal ordering, a model is trained to predict the pace of a video subsampled at different rates. This work also leverages a CSS loss across clips, where positive pairs are clips from the same video and negative pairs are clips from different ones. None of these techniques, however, were designed for pose estimation. For example, predicting temporal order [14, 12, 6, 27] is best suited for activity recognition, for which the order of the observed event truly matters. Similarly, the contrastive learning strategy used in [26] aims to extract features that are invariant across video frames, whereas, to predict a continuously changing body pose, we need to capture variations

between the frames.

Several works have nonetheless focused on extracting time-varying features, yet in different contexts. Harley *et al.* [7] use RGB and depth from n time-steps to map 2.5D feature to a 3D latent space, and then use the camera pose at time-step $n + 1$ to predict the 2D latent features for that time-step. While [7] exploits depth, other works [21, 1, 3] leverage CSS, with [21, 1] using it in single-view videos. However, they do not use any decoder to reconstruct the images from the latent features, thus opening the door to losing valuable information about the observed context. We will demonstrate that for the pose estimation task our encoding/decoding approach yields richer features.

The approach most closely related to ours is DrNet [4], which disentangles each frame into pose and content. DrNet uses a discriminator that distinguishes frames extracted from the same video from ones extracted from different videos and encourages the encoder to produce latent representations that do not carry any information about whether they come from the same or different videos. This, however, fails in cases where the two videos feature different kinds of activities—for example, running in one and sitting on the floor in the other. In this scenario, the pose still indicates if the frames come from the same video or not, which precludes disentanglement.

Multi-View Approaches. The difficulty of performing unsupervised learning using a single camera has led to the development of several multi-view approaches [28, 15, 21, 23, 19, 18]. Among those, the strategy of [19, 18] is closest in spirit to ours. It uses a multi-camera setup to learn a

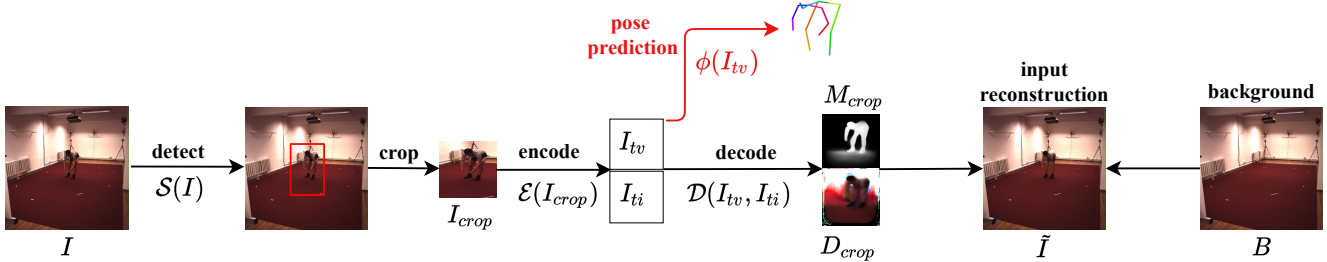


Figure 2. **Model architecture.** Using spatial transformer network (STN) \mathcal{S} , a bounding box is detected and cropped on an input image \mathbf{I} . The cropped image, \mathbf{I}_{crop} , is then passed to an encoder \mathcal{E} that predicts time-invariant \mathbf{I}_{ti} and time-variant \mathbf{I}_{tv} features, which are then passed to a decoder \mathcal{D} that outputs a mask \mathbf{M}_{crop} and RGB crop \mathbf{D}_{crop} . These two outputs are then put to the image resolution using inverse STN operation and then merged with background \mathbf{B} to output the reconstruct image $\tilde{\mathbf{I}}$. This constitutes the self-supervised model, which is then frozen. In the second phase (shown in red), predicted \mathbf{I}_{tv} is passed to a shallow network Φ to predict the pose.

latent-representation that disentangles appearance and pose, where pose should remain similar when rotated across different views and appearance should remain the same across different videos of the same person. This unsupervised training scheme makes it possible to encode an image into a low-dimensional latent vector. As shown in [19, 18], an effective mapping from this latent space to 3D poses can be learned from only a small amount of annotated data. Our approach operates on the same general principle, but we learn the latent representation from videos acquired by a *single* camera, which makes it easier to deploy.

3. Method

Our goal is to extract rich latent features, without any supervision, from single-camera videos featuring people. We aim to capture information only about the foreground subjects and to leverage the similarity or dissimilarity of frames given their distance in time. A key observation is that global object appearance tends to remain constant over time while pose usually changes from frame to frame, which is something our latent vectors should reflect.

To this end, given a video database without annotations, we train an encoder that splits latent features into *time-variant* and *time-invariant* components. The former captures features that remain consistent over time, such as person’s clothing and appearance, while the latter models the time-changing elements in each frame, such as body pose. This enables us to define a similarity measure that accounts for the different behavior of these two components and to implement an effective contrastive-learning procedure that produces latent vectors useful for human pose estimation. Without this split, the latent components learned using similarity measures would be unable to reliably differentiate vectors for temporally away frames, since no matter how distant they are, they still share information.

By contrast, popular approaches to using CSS [16, 1, 21, 3] neither learn time-invariant components nor try to reconstruct the input images. Hence, no decoding occurs

on the learned latent features. We later demonstrate that this approach yields worse results. In other words, splitting latent vectors while leveraging contrastive learning is a unique feature of our approach. Another is an attention mechanism that separates foreground from background and integrates gravity as a supervisory signal when possible. In the remainder of this section, we discuss the different components of our approach in detail.

3.1. Model Architecture and Training

We aim to address real-world applications where the foreground subject is small and occupies only a fraction of the image. To this end, we use a neural network architecture with an attention mechanism to separate foreground from background. As shown in Fig. 2, given an input image \mathbf{I} , a spatial transformer network (STN) \mathcal{S} [11] extracts four parameters that define the subject’s bounding box, two scales s^x, s^y and two translations u^x, u^y , yielding $\mathcal{S}(\mathbf{I}) = (s^x, s^y, u^x, u^y)$. These parameters are used to crop an image patch \mathbf{I}_{crop} that is passed to an encoder \mathcal{E} such that $\mathcal{E}(\mathbf{I}_{crop}) = (\mathbf{I}_{tv}, \mathbf{I}_{ti})$, where \mathbf{I}_{tv} is the time-variant component of the latent vector for image \mathbf{I} and \mathbf{I}_{ti} is the time-invariant component. A decoder \mathcal{D} then takes \mathbf{I}_{tv} and \mathbf{I}_{ti} as inputs and decodes them into a mask \mathbf{M}_{crop} and an RGB crop \mathbf{D}_{crop} . The mask and RGB crops are then used to re-synthesize a full-resolution image by using the inverse transformation of the STN and merging the result with a background image \mathbf{B} . This operation can be written as

$$\tilde{\mathbf{I}} = \mathbf{M} \times \mathbf{D} + (1 - \mathbf{M}) \times \mathbf{B}, \quad (1)$$

where $\tilde{\mathbf{I}}$ is the reconstructed image. Fig. 2 depicts this process. Note that no labels are used here, neither for detection, nor for segmentation. We train networks \mathcal{S} , \mathcal{E} , and \mathcal{D} such that they jointly accomplish three goals:

- Encoding information that relates only to the foreground object;

- Disentangling the time-variant and time-invariant components;
- Encoding time-variant components such that they are more similar for poses that are close in time than for temporally distant ones.

To achieve these goals, we introduce two losses, described in Sections 3.1.1 and 3.1.2, and one training technique discussed in Section 3.1.3.

3.1.1 Reconstruction Loss

To compare the reconstructed image from Eq. (1) with the original one, we use the $L1$ loss expressed as

$$\mathcal{L}_{\text{reconst}} = \|\mathbf{I} - \tilde{\mathbf{I}}\|. \quad (2)$$

As discussed above, we use a background image when re-synthesizing the input image, hence this reconstruction loss encourages our latent representation to focus on the foreground object.

3.1.2 Contrastive Loss

To encourage time-variant components that are close in time to be close to each other and those that are far in time not to be, we rely on a contrastive loss. Many current CSS approaches [3, 16, 1] first take a reference input \mathbf{I} , a positive sample \mathbf{I}^+ , and $n - 1$ negative samples \mathbf{I}_k^- for $1 \leq k < n$, and then minimize the loss

$$\mathcal{L}_{\text{CSS}} = -\log \frac{\exp(\text{sim}(\mathcal{F}(\mathbf{I}), \mathcal{F}(\mathbf{I}^+))/\tau)}{\sum_{k=1}^n \exp(\text{sim}(\mathcal{F}(\mathbf{I}), \mathcal{F}(\mathbf{I}_k^-))/\tau)}, \quad (3)$$

where $\mathcal{F}(\mathbf{I})$ represents the features encoded by the network \mathcal{F} given frame \mathbf{I} as input and $\text{sim}(\mathbf{m}, \mathbf{n}) = (\mathbf{m}^T \mathbf{n}) / (\|\mathbf{m}\| \|\mathbf{n}\|)$. In [21], the contrastive loss is defined instead as a triplet loss

$$\mathcal{L}_{\text{CSS}} = [\|\mathcal{F}(\mathbf{I}) - \mathcal{F}(\mathbf{I}^+)\|^2 + \beta] < \|\mathcal{F}(\mathbf{I}) - \mathcal{F}(\mathbf{I}^-)\|^2, \quad (4)$$

with $\beta > 0$, meaning that the squared L2 distance between a positive pair should be smaller than that between a negative one by at least β . However, neither definition of \mathcal{L}_{CSS} above define the loss relative to the temporal distance of the frames. This is what we change by introducing a distance-based similarity loss.

Distance-based Similarity Loss (DSL). Our goal is to compare every pair of samples directly and to define a loss that enforces similarity or dissimilarity between any two samples depending on their temporal proximity.

Let $\mathbf{I}_{t_v}^m$ and $\mathbf{I}_{t_v}^n$ be the time-variant component of the vectors extracted from two images captured at times t_m and t_n . If $|t_m - t_n|$ is small, we would like $\text{sim}(\mathbf{m}, \mathbf{n})$, where $\text{sim}()$

is the similarity function used in Eq. (3), to be close to one. By contrast, if $|t_m - t_n|$ is larger than a threshold distance d_{max} , we would like $\text{sim}(\mathbf{m}, \mathbf{n})$ to be zero. To this end, we introduce the loss function

$$\mathcal{L}_{\text{DSL}}(\mathbf{I}_{t_v}^m, \mathbf{I}_{t_v}^n) = \begin{cases} (1 - \frac{2d}{d_{\text{max}}}) |\text{sim}(\mathbf{I}_{t_v}^m, \mathbf{I}_{t_v}^n) - 1|, & \text{if } 0 \leq d \leq d_{\text{max}}/2, \\ \min(\frac{2d}{d_{\text{max}}} - 1, 1) |\text{sim}(\mathbf{I}_{t_v}^m, \mathbf{I}_{t_v}^n)|, & \text{otherwise,} \end{cases} \quad (5)$$

where $d = |t_m - t_n|$ is the temporal distance between the two frames. As shown in Fig. 3, \mathcal{L}_{DSL} is piecewise linear in terms of $\text{sim}(\mathbf{I}_{t_v}^m, \mathbf{I}_{t_v}^n)$. It favors similarity for $0 \leq d \leq d_{\text{max}}/2$, and dissimilarity for $d > d_{\text{max}}/2$.

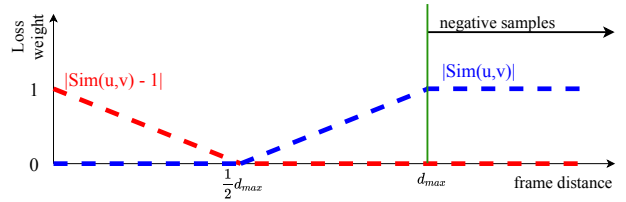


Figure 3. **Distance based Similarity Loss (DSL).** The red line shows the **weight**, $(1 - \frac{2d}{d_{\text{max}}})$, applied to $|\text{sim}(\mathbf{m}, \mathbf{n}) - 1|$ when two frames are close (similarity measure) and the blue line shows the **weight**, $\min(\frac{2d}{d_{\text{max}}} - 1, 1)$, applied to $|\text{sim}(\mathbf{m}, \mathbf{n})|$ when the frames are away (dissimilarity measure). Both weights depend on the temporal distance between the frames. As the frame distance increases, the similarity weight is reduced, eventually going to zero at $d_{\text{max}}/2$, and the dissimilarity weight increases, eventually reaching one at d_{max} , the frame from which negative samples are taken.

In practice, to learn time-variant components in our framework, for any given reference input frame \mathbf{I}^r , we sample three other frames, a nearby one \mathbf{I}^n (positive sample), a far away one \mathbf{I}^a (negative sample taken at least at d_{max}), and an intermediate one, \mathbf{I}^{in} (acquired after \mathbf{I}^n and before \mathbf{I}^a). We then compute

$$\mathcal{L}_{\text{DSL}}^{\text{all}} = \mathcal{L}_{\text{DSL}}(\mathbf{I}_{t_v}^r, \mathbf{I}_{t_v}^n) + \mathcal{L}_{\text{DSL}}(\mathbf{I}_{t_v}^r, \mathbf{I}_{t_v}^a) + \mathcal{L}_{\text{DSL}}(\mathbf{I}_{t_v}^r, \mathbf{I}_{t_v}^{in}). \quad (6)$$

The above loss allows us to compare the reference frame with similar, dissimilar, and intermediate frames directly.

3.1.3 Disentanglement

Note that our DSL only acts on the time-variant components, and thus does not encourage a split between time-variant and time-invariant information. To force the network to disentangle these two types of components, we swap the time-invariant ones across different frames during training. In practice, this means that, at each training iteration, we swap each one of $\{\mathbf{I}_{t_i}^r, \mathbf{I}_{t_i}^n\}$ randomly with one of $\{\mathbf{I}_{t_i}^a, \mathbf{I}_{t_i}^{in}\}$ when reconstructing the synthesized image using Eq. (1). This prevents the time-invariant components from encoding information about the subject’s pose.

3.2. Gravity as a Supervisory Signal

The work reported here was initially motivated by a project that involves modeling competitive divers in free fall. In this context, since the falling person is subject to gravity, we can leverage Newtonian mechanics as follows.

While in free fall, a person’s center of gravity (CG) is subject to gravitational acceleration. Ignoring the air resistance that remains small until the diver reaches the water, $\mathbf{p}(t)$, the CG location at time t , can be written as $\mathbf{p}(t) = 0.5\mathbf{g}t^2 + \mathbf{v}_0t + \mathbf{p}_0$, where \mathbf{g} is a usual gravitational vector, \mathbf{v}_0 the CG initial speed, and \mathbf{p}_0 its initial location. We know neither \mathbf{v}_0 and \mathbf{p}_0 nor when the jump started. Nevertheless, we can leverage the fact that the acceleration, that is, the second derivative of \mathbf{p} is constant and equal to \mathbf{g} . To this end, we only need to consider four *equidistant* times t_1, t_2, t_3, t_4 . We can approximate the acceleration at t_2 and t_3 using finite differences and write that they should be equal. This yields

$$\begin{aligned} 2\mathbf{p}(t_2) - \mathbf{p}(t_1) - \mathbf{p}(t_3) &= 2\mathbf{p}(t_3) - \mathbf{p}(t_2) - \mathbf{p}(t_4) \\ \Rightarrow 3\mathbf{p}(t_2) - 3\mathbf{p}(t_3) + \mathbf{p}(t_4) - \mathbf{p}(t_1) &= 0. \end{aligned} \quad (7)$$

In practice, two difficulties arise in imposing this simple constraint. First, it is not obvious where someone’s CG is given that it depends on their posture and on the weight of each body part. Second, we only have access to 2D projections of $\mathbf{p}(t)$ in the image plane.

Recall from Section 3.1 that our model first applies an STN \mathcal{S} , which, for each frame, outputs a bounding box around the subject parameterized by two scales and two translations, s^x, s^y, u^x, u^y . We address the first problem by approximating the projection of $\mathbf{p}(t)$ as the center of the bounding box. To address the second problem, we consider that the diver’s CG travels in a plane. If it were parallel to the image plane, the value of u^y would vary linearly with the CG height and the relationship of Eq. (7) would hold exactly, implying that

$$3u_2^y - 3u_3^y + u_4^y - u_1^y = 0, \quad (8)$$

where u_t^y denotes the value of u^y at time t . Even when the diver does not travel in a plane parallel to the image one, the frame-to-frame change in distance to the camera of the CG typically remains small and perspective effects are negligible with respect to the vertical motion. Eq.(8) is therefore a good approximation, which we will show in Section S.1 of the supplementary material. We therefore impose the constraint of Eq.(8) as a soft constraint by adding a new loss term into our training procedure.

As shown in the supplementary material, displacement along the x axis occurs but is much smaller than that along the y axis, which we therefore focus on. Hence, we take the new loss term to be

$$\mathcal{L}_{\text{const-acc}} = \|(u_1^y + 3u_2^y) - (u_4^y + 3u_3^y)\|^2, \quad (9)$$

where u_t^y is the translation predicted in the y direction at time t . This definition does not differentiate between moving up or down, whereas, in practice, we know that the diver goes down. In our implementation, this corresponds to u_t^y decreasing. Hence, we also introduce an *order loss* $\mathcal{L}_{\text{order}}$ that we define as

$$\mathcal{L}_{\text{order}} = \sum_{t=1}^3 \max(0, \tau - (u_t^y - u_{t+1}^y)), \quad (10)$$

where τ is a threshold to satisfy a minimum distance between frames t and $t + 1$.

In free-fall, the detector could still make the bounding box bigger to compensate for the aforementioned losses. We therefore prevent the scales s_x and s_y of the bounding boxes from varying abruptly from frame to frame by defining a *scale loss* \mathcal{L}_{sc} as

$$\mathcal{L}_{\text{sc}} = \sum_{t=1}^3 \|(s_t^x, s_t^y) - (s_{t+1}^x, s_{t+1}^y)\|^2. \quad (11)$$

Putting this all together, the tracking loss is then equal to

$$\mathcal{L}_{\text{track}} = \mathcal{L}_{\text{const-acc}} + \mathcal{L}_{\text{order}} + \mathcal{L}_{\text{sc}}. \quad (12)$$

3.3. Training and Inference

To train our network, we adjust the weights of the networks \mathcal{S} , \mathcal{E} , and \mathcal{D} introduced in Section 3.1 to minimize the total training loss

$$\mathcal{L}_{\text{total}} = \mathcal{L}_{\text{reconst}} + \alpha\mathcal{L}_{\text{DSL}}^{\text{all}} + \gamma\mathcal{L}_{\text{track}}, \quad (13)$$

where $\mathcal{L}_{\text{reconst}}$ of Eq. (2) favors a good image reconstruction, $\mathcal{L}_{\text{DSL}}^{\text{all}}$ of Eq. (6) applies a contrastive loss, and $\mathcal{L}_{\text{track}}$ of Eq. (12) is used when the subject is in free fall. During the minimization, we permute randomly the time-invariant components of the latent vectors to promote disentanglement as described in Section 3.1.3. This part of the training is unsupervised.

Once the unsupervised model is trained, its parameters are frozen and we use a small amount of images with corresponding 3D poses for supervised training of a simple two-layer perception Φ designed to associate a pose vector to the time-variant latent vector $\mathbf{I}_{\mathbf{tv}}$ that the encoder \mathcal{E} has extracted from image \mathbf{I} . To this end we adjust the weights of Φ by minimizing

$$\mathcal{L}_{\text{pose}} = \frac{1}{N} \sum_{k=1}^N \|\Phi(\mathbf{I}_{\mathbf{tv}}^k) - \mathbf{p}^k\|^2, \quad (14)$$

where $\mathbf{I}_{\mathbf{tv}}^k$ is the time-variant vector associated to the k^{th} image and \mathbf{p}^k the corresponding ground-truth pose, in camera-coordiante and pelvis centered, represented by a concatenation of the Cartesian coordinates of body joints.

4. Experimental Results

In this section, we present the baseline models and compare our approach to these models on 3D human pose estimation. Please check the supplementary material for model architecture and experimental details.

4.1. Baseline Models

We compare our model to the following baselines:

- **CSS [1, 3]:** Single-view CSS loss using Eq. (3) without image reconstruction or splitting the latent space into \mathbf{I}_{t_v} and \mathbf{I}_{t_i} components.
- **MV-CSS [21]:** Multi-view CSS loss using the triplet loss of Eq. (4), also without reconstruction or splitting.
- **DrNet [4]:** Single-view approach using both reconstruction and latent splitting. It uses a discriminator for latent splitting.
- **NSD [18]:** Multi-view approach that performs both reconstruction and latent splitting.

and against variants of our own approach:

- **AE-STN:** This is a variant of our model that uses STN together with an auto-encoding image-reconstruction, without contrastive training or latent splitting.
- **CSS-STN:** This is a variant of our model that uses STN together with image-reconstruction and latent splitting. However, we use Eq. (3) instead of Eq. (5) for the contrastive loss.
- **CSS-DSL:** This is our approach using STN together with image-reconstruction and latent splitting. It uses Eq. (5) for the contrastive loss.

All of these models are trained with the same backbone architecture and model capacity, so that only the training loss differentiates them. For MV-CSS, we follow the recommendation in [21] to sample one positive sample from another view at the same timestamp, and one negative sample from a distant frame in the same video. For CSS and CSS-STN, we use one positive sample from a nearby-frame and two negative samples from away frames from the same video. For DSL-STN, we replace one of the away frames with an intermediate frame, sampled between nearby and away frames. We follow the procedures given in [4, 18] to train DrNet and NSD.

4.2. 3D Pose Prediction Results

For all models, given the latent representation learned in a self-supervised manner, we train an MLP with 2 hidden layers taking a latent vector as input, as discussed in Section 3.3. At this stage, the self-supervised models are frozen

and only the pose models are trained. For the models that split the latent features, we use the time-variant component for pose estimation. For the models that don't, we use all latent features. We report the results using the normalized mean per joint position error (N-MPJPE), expressed in mm.

4.2.1 Human3.6M [10] (H36M)

Following the protocol of [18], we use subjects S1, S5, S6, S7, S8 to train the self-supervised models. We subsample every 5 frames of the training set, as done in [18], which yields 308,760 frames.

Comparison with other models. We follow the same procedure as in [18] for 3D human pose estimation within the PoseTrack2018 challenge setup. It comprises 35,832 training images with pose labels and 19,312 test samples. We compare our results to those of other unsupervised models in Table 1 and report the N-MPJPE as a function of the percentage of labeled pose samples being used. We consistently outperform the other single-view methods and come close to NSD, even though it uses multiple views. Note that the models without decoding, whether single- or multi-view perform poorly on this task.

Ablation Study. We perform an ablation study by removing different components of our model. The results are shown in Table 2 in the same experimental setup as in Table 1.

In the first two rows, we remove the reconstruction loss and only train the model with the DSL loss term. The performance drops considerably, indicating the importance of image reconstruction in learning rich features. Since the model does not reconstruct the image, it cannot learn the time-invariant components, so all the latent components are time-variant. The number of latent features in these models are equivalent to that in the model that uses time-variant and time-invariant features, so there is no capacity change.

In the third row, we have a model that reconstructs the input but does not apply a latent split. The performance is also reduced, showing that splitting the latent space is beneficial in learning better time-variant features. Finally, in the fourth row, we change only the DSL loss of Eq. (5) to the CSS loss in Eq. (3) and still observe a performance drop. In summary, all the proposed modules have a role and disabling any of them reduces performance.

4.2.2 MPI-INF-3DHP [13] (MPI)

On this dataset, we consider two settings:

1. MV-data: The self-supervised model is trained on subjects S1 to S8, which are multi-view. Since the test-videos have different background compared to the training videos, we train the self-supervised models on

	Model	Decodes?	Percentage of Labeled Pose Data				
			0.3% (100)	1% (500)	14% (5K)	50% (17K)	all (35K)
Multi-View	MV-CSS [21]	✗	216.15	206.08	203.24	202.65	202.52
	NSD [18]	✓	140.92	115.37	94.48	91.01	88.89
Single-View	CSS [1, 3]	✗	230.77	215.96	197.22	195.70	194.69
	DrNet [4]	✓	158.81	126.18	108.21	106.41	100.38
	AE-STN	✓	178.60	147.21	117.28	112.38	111.09
	CSS-STN	✓	160.45	132.40	105.77	99.23	98.25
	DSL-STN (Ours)	✓	148.61	121.30	99.36	93.79	93.99

Table 1. **Comparison against baselines on the PoseTrack H36M test-set.** The top rows characterize the unsupervised multi-view models and the bottom rows the single-view ones. The last 5 columns show N-MPJPE results when using different percentage of labeled 3D pose samples. The value in parenthesis are the corresponding number of images with labels.

Decodes?	uses STN?	contrastive loss	latent split?	Percentage of Labeled Pose Data				
				0.3% (100)	1% (500)	14% (5K)	50% (17K)	all (35K)
✗	✗	DSL	✗	228.82	210.29	196.84	194.27	192.03
✗	✓	DSL	✗	232.19	212.91	200.33	200.07	199.69
✓	✓	DSL	✗	185.75	159.34	135.93	129.62	127.52
✓	✓	CSS	✓	160.45	132.40	105.77	99.23	98.25
✓	✓	DSL	✓	148.61	121.30	99.36	93.79	93.99

Table 2. **Ablation Study.** The last row shows our full model with all features applied. In the first two rows we remove the decoding part. In this setting since the model is not reconstructing the image from the latent features it can only learn the time-variant features, hence the latent-split cannot be applied. In the third row, we keep all the features except we do not split the latent components. In the fourth row, we only change the contrastive loss from DSL to CSS. In all settings, we observe a performance drop, however, the models without decoding suffer the most.

random image backgrounds to help the model generalize to new backgrounds. To this end, we take random images from the Internet as background and put the subject in-front of them, using the foreground mask of the dataset. Note that these masks are not used for training the models.

- All-data: Since the self-supervised models do not require labels, we can leverage all data to train them, whether single or multi-view. This corresponds to a transductive learning setting. In this case, the self-supervised model is trained using S1 to S8 (multi-view) and TS1 to TS4 (single-view).

The datasets are subsampled every 5 frames, yielding 198,096 training frames in the MV-data case and 202,905 training frames in all-data case.

In both settings, to train the pose estimation MLP, we use subjects S1, S2, S3, S4, S5, S8 as train-set, and S6 and S7 as validation-set. For testing, we use TS1 to TS4. Because there are many pose labels, we use at most 2% of the pose data for training, that is, 17,128 images. The test set comprises 2207 frames. We report the results in Table 3. As the S1 to S8 videos are multi-view and the TS1 to TS4 ones are single-view, we can only evaluate NSD in the MV-data setting. Our model again performs closely to NSD in this setting with the advantage that, because our approach is single-view, we can also train on the TS1 to TS4

videos, thus further improving performance. In a practical setting, this means that we could exploit additional videos as they become available, whether or not they are multi-view, something NSD cannot do.

	Model	Percentage of Labeled Pose Data				
		.02% (171)	.1% (856)	.2% (1712)	5% (4K)	2% (17K)
MV-data	AE-STN	279.00	258.73	256.27	251.92	246.57
	CSS-STN	274.45	255.91	252.45	246.64	242.92
	NSD [18]	256.34	241.12	239.81	237.56	235.61
	DSL-STN (Ours)	261.99	245.09	241.34	239.48	236.85
All-data	AE-STN	245.87	230.98	225.42	220.19	206.98
	CSS-STN	243.83	223.85	218.62	208.25	203.69
	DrNet [4]	253.47	243.87	233.09	228.09	218.18
	DSL-STN (Ours)	235.62	219.72	211.26	202.60	192.11

Table 3. **Comparing against baselines on MPI-INF-3DHP.** N-MPJPE results on pose prediction as a function of the quantity of annotated data. The top rows show results in the MV-data setting, where the self-supervised models have access only to multi-view data. The bottom rows show results in the All-data setting where self-supervised models have access to both multi-view and single-view data. Note that, in this scenario, our results are now better than those of NSD because it can also exploit single-view data.

4.2.3 Diving Dataset

We acquired video sequences featuring a male and a female competitive divers. The dataset contains dives with heights of 3, 5, 7.5, and 10 meters, and is captured with both multi-camera and single-camera setups. We use both subjects to train the self-supervised model, yielding 19,464 training frames, of which 16,469 frames are multi-view. NSD

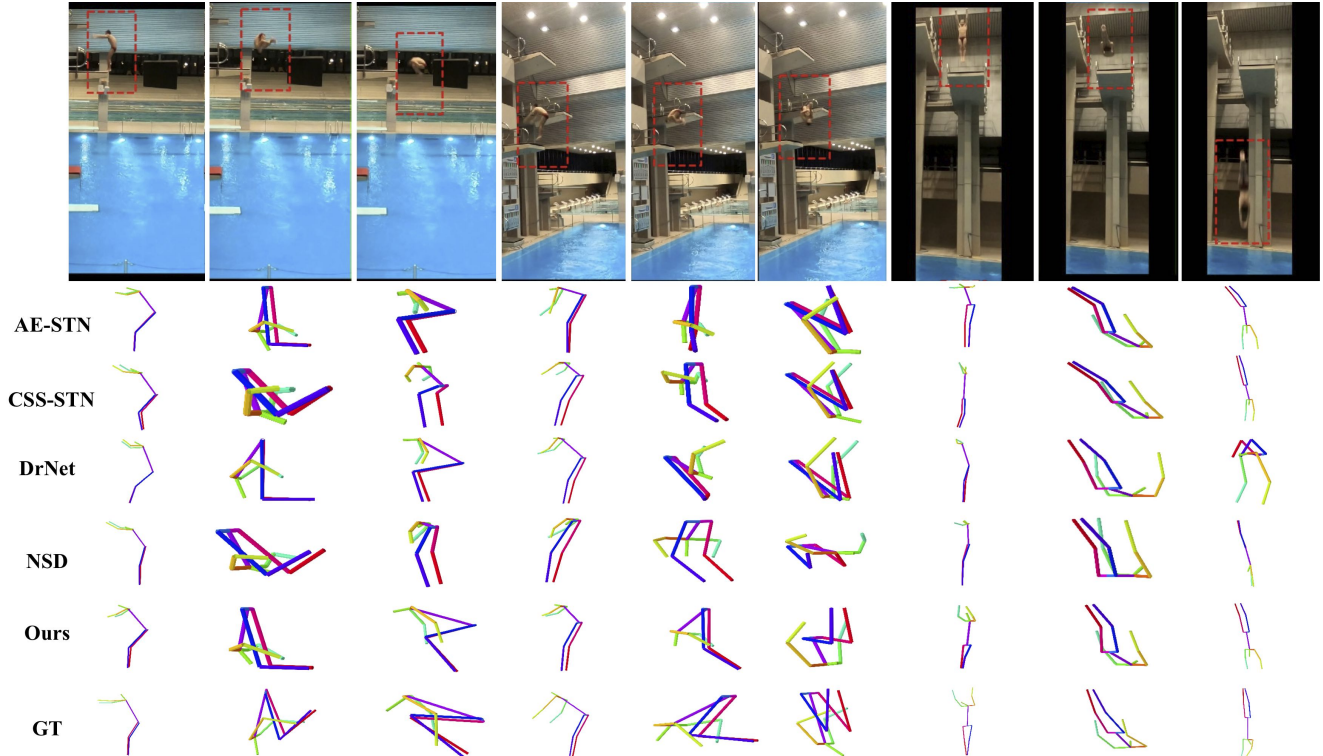


Figure 4. **Qualitative results on the Diving Dataset.** Samples are taken from the test set at different stages of dive. The red region shows the bounding box detected by our model for image cropping. GT in the bottom row indicates the ground truth labels.

is trained on multi-view videos while all other models are trained on all frames.

To train the pose model, for all models we use the female subject for training, by splitting the videos into training and validation sets, and the male for testing. As a result, we can use up to 2,419 frames for supervised training, 2,288 frame for validation, and 2,112 frames for testing. We report the accuracy of the models in Table 4. On this dataset, our approach outperforms all the other methods including the multi-view NSD. While NSD model can only leverage multi-view videos, our approach can leverage both multi and single-view, hence it can leverage more available data. It also outperforms the variant AE-STN and CSS-STN, thus confirming the conclusions of the ablation study of Section 4.2.1. We show some pose prediction results in Fig. 4. Check the supplementary material for further visualization.

Model		Percentage of Labeled Pose Data				
		5% (120)	10% (241)	20% (483)	50% (1209)	100% (2419)
Multi-View	NSD [18]	300.47	269.70	254.28	234.77	227.13
	DSL-STN (Ours)	293.80	268.94	247.02	226.89	222.07
All-data	AE-STN	320.93	295.65	277.96	266.64	257.19
	CSS-STN	311.15	284.29	267.27	247.28	238.87
	DrNet [4]	320.07	290.93	271.87	258.14	248.31
	DSL-STN (Ours)	287.18	251.92	233.92	224.55	215.71

Table 4. **Comparison against baselines on the Diving dataset.** N-MPJPE results as a function of the quantity of annotated data used to train the pose predictor. Top two rows show models trained only on multi-view data. The bottom rows show models trained using both single-view and multi-view data.

5. Conclusion

In this work, we have presented an unsupervised feature extraction model for monocular videos. It focuses contrastive learning to the time-variant components of the input, which, together with an additional image decoding, allows it to extract richer features than standard CSS approaches. Our framework is designed to extract features from the foreground object, and is thus well-suited to 3D human pose estimation. We have evidenced this on three benchmark datasets where our approach was shown to outperform other single-view self-supervised learning strategies and to match the performance of multi-view ones. Nevertheless, our approach is not restricted to human pose estimation, and we will study its use for other tasks.

Acknowledgment. This work was supported in part by Innosuisse, the Swiss Innovation Agency. We also would like to thank SwissTiming for their support and cooperation in this project.

References

- [1] Ankesh Anand, Evan Racah, Sherjil Ozair, Yoshua Bengio, Marc-Alexandre Côté, and R Devon Hjelm. Unsupervised state representation learning in atari. In *Advances in Neural*

- Information Processing Systems*, pages 8769–8782, 2019. [1](#), [2](#), [3](#), [4](#), [6](#), [7](#)
- [2] Y. Bengio, A. Courville, and P. Vincent. Representation Learning: A Review and New Perspectives. *IEEE Transactions on Pattern Analysis and Machine Intelligence*, 2013. [2](#)
- [3] Ting Chen, Simon Kornblith, Mohammad Norouzi, and Geoffrey Hinton. A simple framework for contrastive learning of visual representations. *International Conference on Machine Learning*, 2020. [1](#), [2](#), [3](#), [4](#), [6](#), [7](#)
- [4] Emily L Denton et al. Unsupervised learning of disentangled representations from video. In *Advances in Neural Information Processing Systems*, pages 4414–4423, 2017. [2](#), [6](#), [7](#), [8](#)
- [5] C. Doersch and A. Zisserman. Multi-Task Self-Supervised Visual Learning. In *International Conference on Computer Vision*, October 2017. [2](#)
- [6] Basura Fernando, Hakan Bilen, Efstratios Gavves, and Stephen Gould. Self-supervised video representation learning with odd-one-out networks. In *Conference on Computer Vision and Pattern Recognition*, pages 3636–3645, 2017. [2](#)
- [7] Adam W. Harley, Shrinidhi K. Lakshmikanth, Fangyu Li, Xian Zhou, Hsiao-Yu Fish Tung, and Katerina Fragkiadaki. Learning from unlabelled videos using contrastive predictive neural 3d mapping. In *International Conference on Learning Representations*, 2020. [2](#)
- [8] K. He, X. Zhang, S. Ren, and J. Sun. Deep Residual Learning for Image Recognition. In *Conference on Computer Vision and Pattern Recognition*, pages 770–778, 2016. [10](#)
- [9] Aapo Hyvarinen and Hiroshi Morioka. Unsupervised feature extraction by time-contrastive learning and nonlinear ica. In *Advances in Neural Information Processing Systems*, pages 3765–3773, 2016. [1](#)
- [10] C. Ionescu, J. Carreira, and C. Sminchisescu. Iterated Second-Order Label Sensitive Pooling for 3D Human Pose Estimation. In *Conference on Computer Vision and Pattern Recognition*, 2014. [6](#)
- [11] M. Jaderberg, K. Simonyan, A. Zisserman, and K. Kavukcuoglu. Spatial Transformer Networks. In *Advances in Neural Information Processing Systems*, pages 2017–2025, 2015. [3](#)
- [12] Hsin-Ying Lee, Jia-Bin Huang, Maneesh Singh, and Ming-Hsuan Yang. Unsupervised representation learning by sorting sequences. In *Conference on Computer Vision and Pattern Recognition*, pages 667–676, 2017. [2](#)
- [13] D. Mehta, H. Rhodin, D. Casas, P. Fua, O. Sotnychenko, W. Xu, and C. Theobalt. Monocular 3D Human Pose Estimation in the Wild Using Improved CNN Supervision. In *International Conference on 3D Vision*, 2017. [6](#)
- [14] Ishan Misra, C Lawrence Zitnick, and Martial Hebert. Shuffle and learn: Unsupervised learning using temporal order verification. In *European Conference on Computer Vision*, pages 527–544, 2016. [2](#)
- [15] Joel Ruben Antony Moniz, Christopher Beckham, Simon Rajotte, Sina Honari, and Chris Pal. Unsupervised depth estimation, 3d face rotation and replacement. In *Advances in Neural Information Processing Systems*, pages 9736–9746, 2018. [2](#)
- [16] Aaron van den Oord, Yazhe Li, and Oriol Vinyals. Representation learning with contrastive predictive coding. In *arXiv Preprint*, 2018. [1](#), [3](#), [4](#)
- [17] G. Pavlakos, X. Zhou, K. Derpanis, G. Konstantinos, and D. Kostas. Harvesting Multiple Views for Marker-Less 3D Human Pose Annotations. In *Conference on Computer Vision and Pattern Recognition*, 2017. [1](#)
- [18] H. Rhodin, V. Constantin, I. Katircioglu, M. Salzmann, and P. Fua. Neural Scene Decomposition for Human Motion Capture. In *Conference on Computer Vision and Pattern Recognition*, 2019. [1](#), [2](#), [3](#), [6](#), [7](#), [8](#), [10](#)
- [19] H. Rhodin, M. Salzmann, and P. Fua. Unsupervised Geometry-Aware Representation for 3D Human Pose Estimation. In *European Conference on Computer Vision*, 2018. [2](#), [3](#)
- [20] H. Rhodin, J. Spoerri, I. Katircioglu, V. Constantin, F. Meyer, E. Moeller, M. Salzmann, and P. Fua. Learning Monocular 3D Human Pose Estimation from Multi-View Images. In *Conference on Computer Vision and Pattern Recognition*, 2018. [1](#)
- [21] Pierre Sermanet, Corey Lynch, Yevgen Chebotar, Jasmine Hsu, Eric Jang, Stefan Schaal, Sergey Levine, and Google Brain. Time-contrastive networks: Self-supervised learning from video. In *International Conference on Robotics and Automation*, pages 1134–1141, 2018. [1](#), [2](#), [3](#), [4](#), [6](#), [7](#)
- [22] Nitish Srivastava, Elman Mansimov, and Ruslan Salakhudinov. Unsupervised learning of video representations using lstms. In *International Conference on Machine Learning*, pages 843–852, 2015. [2](#)
- [23] Z. Tian, C. Shen, H. Chen, and T. He. FCOS: Fully Convolutional One-Stage Object Detection. In *Conference on Computer Vision and Pattern Recognition*, 2019. [2](#)
- [24] H.-Y. Tung, H.-W. Tung, E. Yumer, and K. Fragkiadaki. Self-Supervised Learning of Motion Capture. In *Advances in Neural Information Processing Systems*, pages 5242–5252, 2017. [1](#)
- [25] Jiangliu Wang, Jianbo Jiao, Linchao Bao, Shengfeng He, Yunhui Liu, and Wei Liu. Self-supervised spatio-temporal representation learning for videos by predicting motion and appearance statistics. In *Conference on Computer Vision and Pattern Recognition*, pages 4006–4015, 2019. [2](#)
- [26] J. Wang, J. Jiao, and Y. Liu. Self-Supervised Video Representation Learning by Pace Prediction. In *European Conference on Computer Vision*, 2020. [2](#)
- [27] Dejing Xu, Jun Xiao, Zhou Zhao, Jian Shao, Di Xie, and Yueting Zhuang. Self-supervised spatiotemporal learning via video clip order prediction. In *Conference on Computer Vision and Pattern Recognition*, pages 10334–10343, 2019. [2](#)
- [28] T. Zhou, M. Brown, N. Snavely, and D. Lowe. Unsupervised Learning of Depth and Ego-Motion from Video. In *Conference on Computer Vision and Pattern Recognition*, pages 1851–1858, 2017. [1](#), [2](#)

Unsupervised Learning on Monocular Videos for 3D Human Pose Estimation

Supplementary Information

S.1. Projected Gravity Acceleration

An object's location $\mathbf{p}(t)$ at time t falling down in 3D space using gravity is formulated by $\mathbf{p}(t) = 0.5\mathbf{g}t^2 + \mathbf{v}_0t + \mathbf{p}_0$, where \mathbf{g} , \mathbf{v}_0 , and \mathbf{p}_0 respectively indicating initial speed, initial location and gravity. We can write the projection of the center of gravity CG in the image plane in projective coordinates as

$$\mathbf{p}_{\text{proj}} = [p_{\text{proj}}^x, p_{\text{proj}}^y, p_{\text{proj}}^z] = \mathbf{K}[\mathbf{R}|\mathbf{T}](0.5\mathbf{g}t^2 + \mathbf{v}_0t + \mathbf{p}_0), \quad (15)$$

where \mathbf{g} , \mathbf{v}_0 , and \mathbf{p}_0 are represented in homogeneous coordinates, each being a column vector of 4×1 . this yields

$$\begin{bmatrix} p_{\text{proj}}^x \\ p_{\text{proj}}^y \\ p_{\text{proj}}^z \end{bmatrix} = \begin{bmatrix} \mathbf{K}_1^T[\mathbf{R}|\mathbf{T}](0.5\mathbf{g}t^2 + \mathbf{v}_0t + \mathbf{p}_0) \\ \mathbf{K}_2^T[\mathbf{R}|\mathbf{T}](0.5\mathbf{g}t^2 + \mathbf{v}_0t + \mathbf{p}_0) \\ \mathbf{K}_3^T[\mathbf{R}|\mathbf{T}](0.5\mathbf{g}t^2 + \mathbf{v}_0t + \mathbf{p}_0) \end{bmatrix} \quad (16)$$

where \mathbf{K}_i^T is the i -th row of matrix \mathbf{K} . The observed x and y locations are then equal to

$$p^x = p_{\text{proj}}^x / p_{\text{proj}}^z, \quad p^y = p_{\text{proj}}^y / p_{\text{proj}}^z.$$

When the image plane is parallel to the plane in which the subject travels, the depth p_{proj}^z remains fixed in the course of dive, so we can treat it as a constant c . In this case, we then get

$$\begin{bmatrix} p^x \\ p^y \end{bmatrix} = \frac{1}{c} \begin{bmatrix} \mathbf{K}_1^T[\mathbf{R}|\mathbf{T}](0.5\mathbf{g}t^2 + \mathbf{v}_0t + \mathbf{p}_0) \\ \mathbf{K}_2^T[\mathbf{R}|\mathbf{T}](0.5\mathbf{g}t^2 + \mathbf{v}_0t + \mathbf{p}_0) \end{bmatrix} \quad (17)$$

Getting the second order derivative yields

$$\begin{bmatrix} a^x \\ a^y \end{bmatrix} = \frac{1}{c} \begin{bmatrix} \mathbf{K}_1^T[\mathbf{R}|\mathbf{T}]\mathbf{g} \\ \mathbf{K}_2^T[\mathbf{R}|\mathbf{T}]\mathbf{g} \end{bmatrix} \quad (18)$$

with a^x and a^y being acceleration in x and y directions. This makes acceleration a constant value of intrinsic \mathbf{K} , rotation \mathbf{R} , translation \mathbf{T} , and gravity \mathbf{g} , hence not a function of time t . In this case, our assumption strictly holds.

On the other hand, if the subject travels on a plane not parallel to the image plane, the depth of observed location changes over time, making it a function of t . In this case for y location we have (p^x is obtained similarly)

$$p^y = \frac{p_{\text{proj}}^y}{p_{\text{proj}}^z} = \frac{\mathbf{K}_2^T[\mathbf{R}|\mathbf{T}](0.5\mathbf{g}t^2 + \mathbf{v}_0t + \mathbf{p}_0)}{\mathbf{K}_3^T[\mathbf{R}|\mathbf{T}](0.5\mathbf{g}t^2 + \mathbf{v}_0t + \mathbf{p}_0)} \quad (19)$$

Getting derivative w.r.t t we have

$$v^y = \frac{\partial p^y}{\partial t} = \frac{\mathbf{K}_2^T[\mathbf{R}|\mathbf{T}](\mathbf{g}t + \mathbf{v}_0)(p_{\text{proj}}^z) - \mathbf{K}_3^T[\mathbf{R}|\mathbf{T}](\mathbf{g}t + \mathbf{v}_0)(p_{\text{proj}}^y)}{(p_{\text{proj}}^z)^2} = \frac{(p_{\text{proj}}^z \mathbf{K}_2^T - p_{\text{proj}}^y \mathbf{K}_3^T)([\mathbf{R}|\mathbf{T}](\mathbf{g}t + \mathbf{v}_0))}{(p_{\text{proj}}^z)^2} \quad (20)$$

Getting second derivative w.r.t t we obtain

$$a^y = \frac{\partial v^y}{\partial t} = \frac{(p_{\text{proj}}^z \mathbf{K}_2^T - p_{\text{proj}}^y \mathbf{K}_3^T)([\mathbf{R}|\mathbf{T}]\mathbf{g})(p_{\text{proj}}^z)^2}{(p_{\text{proj}}^z)^4} - \frac{2p_{\text{proj}}^z (\frac{\partial}{\partial t} p_{\text{proj}}^z)(p_{\text{proj}}^z \mathbf{K}_2^T - p_{\text{proj}}^y \mathbf{K}_3^T)([\mathbf{R}|\mathbf{T}](\mathbf{g}t + \mathbf{v}_0))}{(p_{\text{proj}}^z)^4} = \frac{p_{\text{proj}}^z (p_{\text{proj}}^z \mathbf{K}_2^T - p_{\text{proj}}^y \mathbf{K}_3^T)[\mathbf{R}|\mathbf{T}](p_{\text{proj}}^z \mathbf{g} - (2(\frac{\partial}{\partial t} p_{\text{proj}}^z)(\mathbf{g}t + \mathbf{v}_0)))}{(p_{\text{proj}}^z)^4} \quad (21)$$

As can be seen in the last line of Eq.(21), both the nominator and denominator depend on p_{proj}^z , which is the depth. It changes over time and is therefore a function of t . This violates our assumption that the acceleration is constant in the image plane when the subject moves in a plane not parallel to the image plane. However, p_{proj}^z only changes slowly for points far away from the camera because perspective projection gets increasingly close to orthographic projection as one moves away from the camera.

S.2. Model Architecture and Training

We use an input image resolution of size 500×500 in H36 and MPI datasets, and 500×1000 in Diving dataset. To implement the STN \mathcal{S} of Section. 3.1, we use a ResNet18 [8] that takes as input, the input image downsampled by a factor 4 in both dimensions and returns $\mathcal{S}(\mathbf{I}) = (s^x, s^y, u^x, u^y)$. This is used to crop a patch \mathbf{I}_{crop} that is then resized to 128×128 using the affine-grid function of pyTorch. As in [18], we use a pre-trained ResNet50 [8] model as the encoder \mathcal{E} . In the decoder \mathcal{D} , \mathbf{I}_{tv} features are first passed to a fully-connected layer with ReLU and dropout with an output size of 32,768, which is then reshaped to 128 feature maps of resolution 16×16 . The \mathbf{I}_{ti} features are passed to another fully-connected layer with ReLU and dropout to produce an output of shape 128×16^2 . The two feature maps are then concatenated into a feature map of

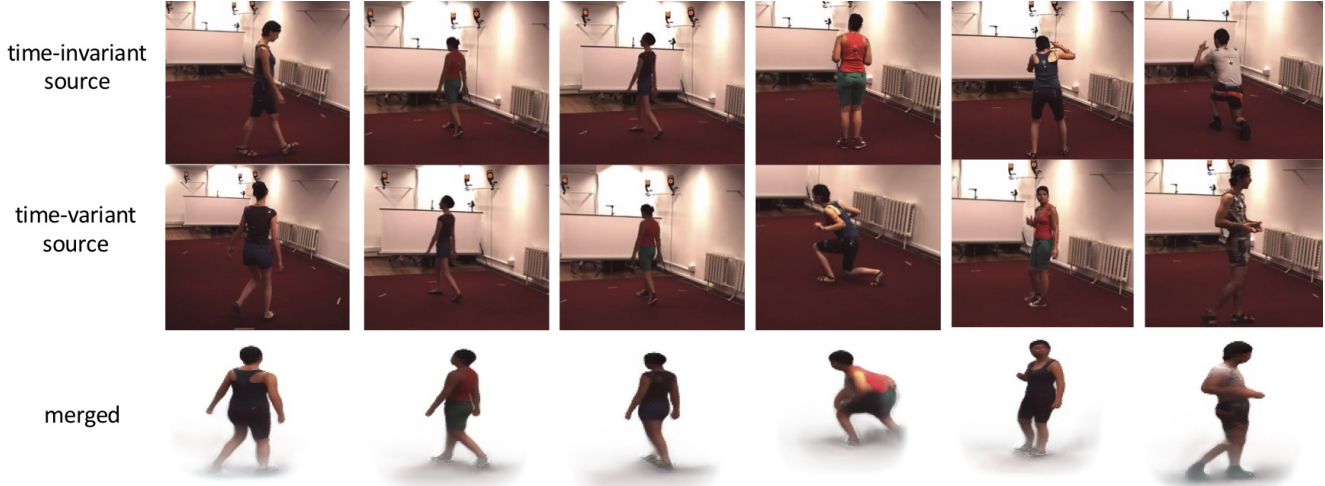


Figure S1. **Swapping time-invariant and time-variant components.** In each column, the time-invariant component is taken from the image on the top, and the time-variant component is taken from the image on the bottom and concatenated to generate the image shown in bottom, using the decoder.



Figure S2. **Swapping time-invariant and time-variant components.** In each column, the time-invariant component is taken from the image on the top, and the time-variant component is taken from the image on the bottom and concatenated to generate the image shown in bottom, using the decoder. In the last example, on the right, we show an example where the model does not completely separate the time-invariant and time-variant components and the shirt of the output image resembles the one of the time-variant sample.

size 256×16^2 . This feature map is then passed to three upsampling layers with, each with one bilinear upsampling with factor 2 and three convolutional layers with kernel size 3×3 . This upsamples the feature maps from 256×16^2 , in order, to 128×32^2 , 64×64^2 , and finally to 32×128^2 . A final convolutional layer is then applied to make the resolution of these feature maps 4×128^2 , where the first three channels are the decoded image crop D_{crop} and the last channel is the foreground subject mask crop M_{crop} . Finally, the inverse STN function is used to map the resolution of D_{crop} and M_{crop} to that of the original image and reconstructing the final image \tilde{I} according to Eq.(1).

In practice, we can train this model by simply minimiz-

ing the total loss of $\mathcal{L}_{\text{total}}$ of Eq.(13). However, convergence is very slow because it takes a long time for the STN to find the right locations for the bounding boxes. To speed up convergence, we therefore introduce priors for the bounding box locations.

H36M. and MPI. We apply a Gaussian prior on the location and size of the bounding box. We set the average detected size of the bounding box, over the mini-batch, to be about 50% of the input image resolution. On H36M we also set a prior that the location of the detected bounding box should, on average over mini-batch, be in the middle of the frame. The latter is not needed on MPI. Note that these priors are applied to the average prediction and not individ-



Figure S3. **Qualitative results on H36M Dataset.** Samples are taken from the test set. In the top row, the red rectangle shows the bounding box detected by our model for image cropping. The two bottom rows, respectively show the pose estimation by our model and the ground truth pose. The last two columns show examples with high error.

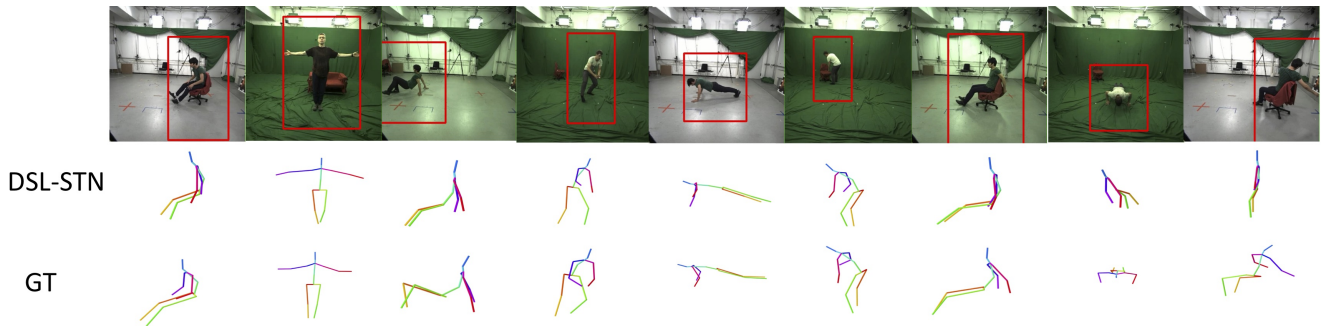


Figure S4. **Qualitative results on MPI Dataset.** Samples are taken from the test set. In the top row, the red rectangle shows the bounding box detected by our model for image cropping. The two bottom rows, respectively show the pose estimation by our model and the ground truth pose. The last two columns show examples with high error.

ual ones, which would otherwise imply a strong bias.

Diving. On this free-fall motion, we use the gravity loss introduced in Section 3.2 in addition to the other objectives. It requires sampling frames that are temporally equidistant. Since this sampling is different from the one required for the CSS terms and the mini-batch size is limited, we propose a two-stage training strategy. First, the network is pre-trained with $\mathcal{L}_{\text{DSL}}^{\text{all}}$ with CSS disabled, which helps the network on the difficult task of localizing the small diver in the full-frame image. Second, we switch to CSS loss $\mathcal{L}_{\text{DSL}}^{\text{all}}$ and its sampling for learning a precise human model for which the gravity loss is no longer required.

We do not apply any data-augmentation for training either the self-supervised model or the pose estimation model. Regarding hyper-parameters, we set γ to 1 in the Diving dataset and α to 0.1 on H36M and MPI dataset, and to 0.01 on the diving dataset. We used the following temporal distance for sampling in models that use contrastive loss: In H36M, we used a maximum of 10 temporal frame distance for positive samples and a minimum of 200 for negative samples. In MPI, we used 10 for positive and 450 for negative samples. In Diving dataset, as poses change very quickly within few frames, we used 3 for positive sam-

ples, and 20 for negative samples. These hyper-parameters were selected based on how fast the poses change in the videos and the quality of image-reconstruction in the self-supervised models, which is our early-stopping criteria in the self-supervised model. We used the same sampling procedure for all models that use a contrastive loss.

S.3. Disentanglement

In Figures S1 and S2 we take time-invariant component from an image and time-variant component from a different image to reconstruct an output image. As can be observed, the model learns to separate these two components.

S.4. Qualitative Results

In Figures S3 and S4 we show pose estimation results on H36M and MPI test set. In Figures S5, S6, and S7 we show samples on the Diving dataset.

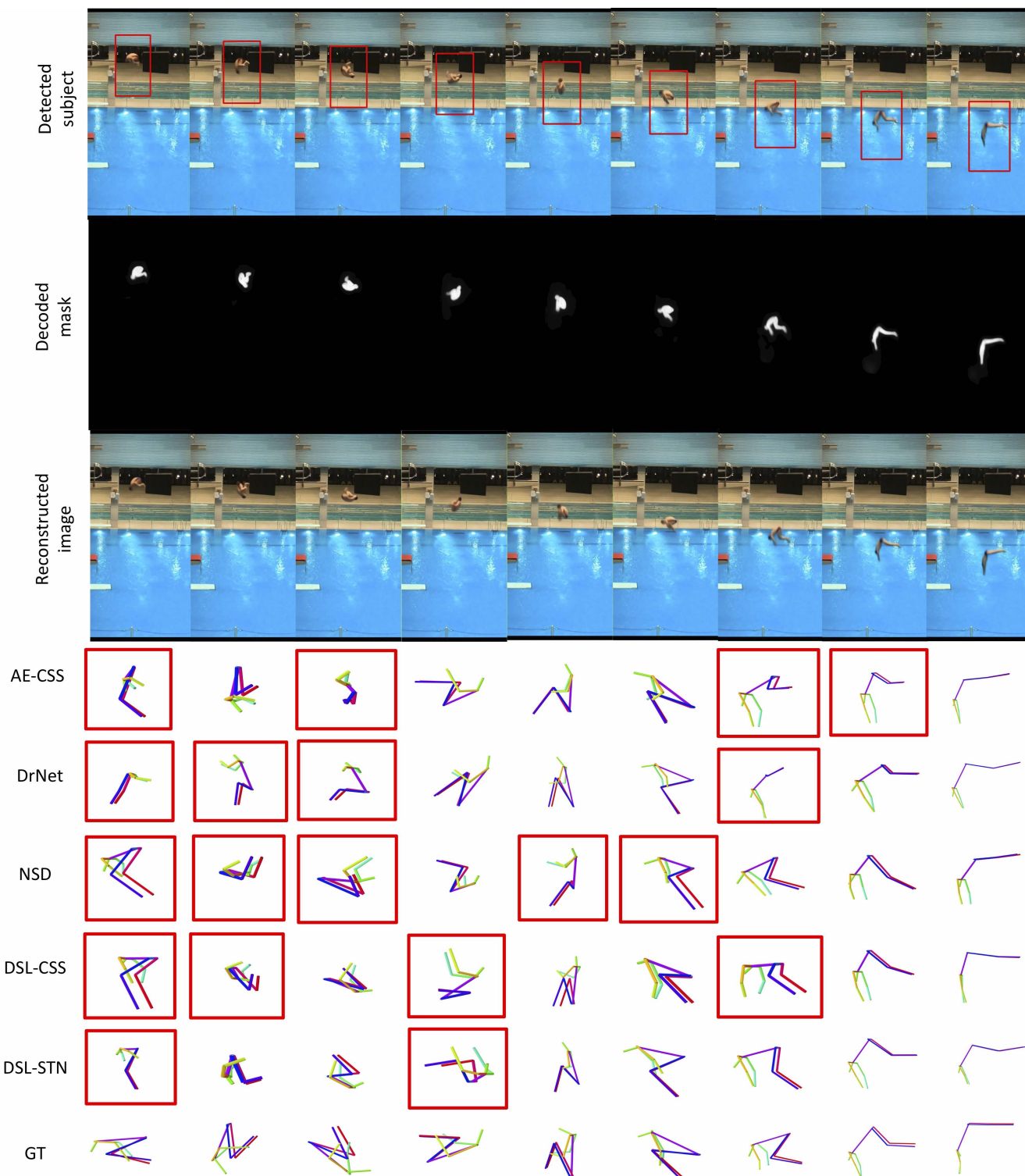


Figure S5. **Qualitative results on Diving Dataset.** Samples are taken from the test set. In the top row, the red rectangle shows the bounding box detected by our model for image cropping. The second and third rows, show respectively the decoded mask and image. Bottom rows, show the pose estimation by different models, where the red rectangle indicates pose estimation with a high error. GT in the bottom row indicates the ground truth labels.

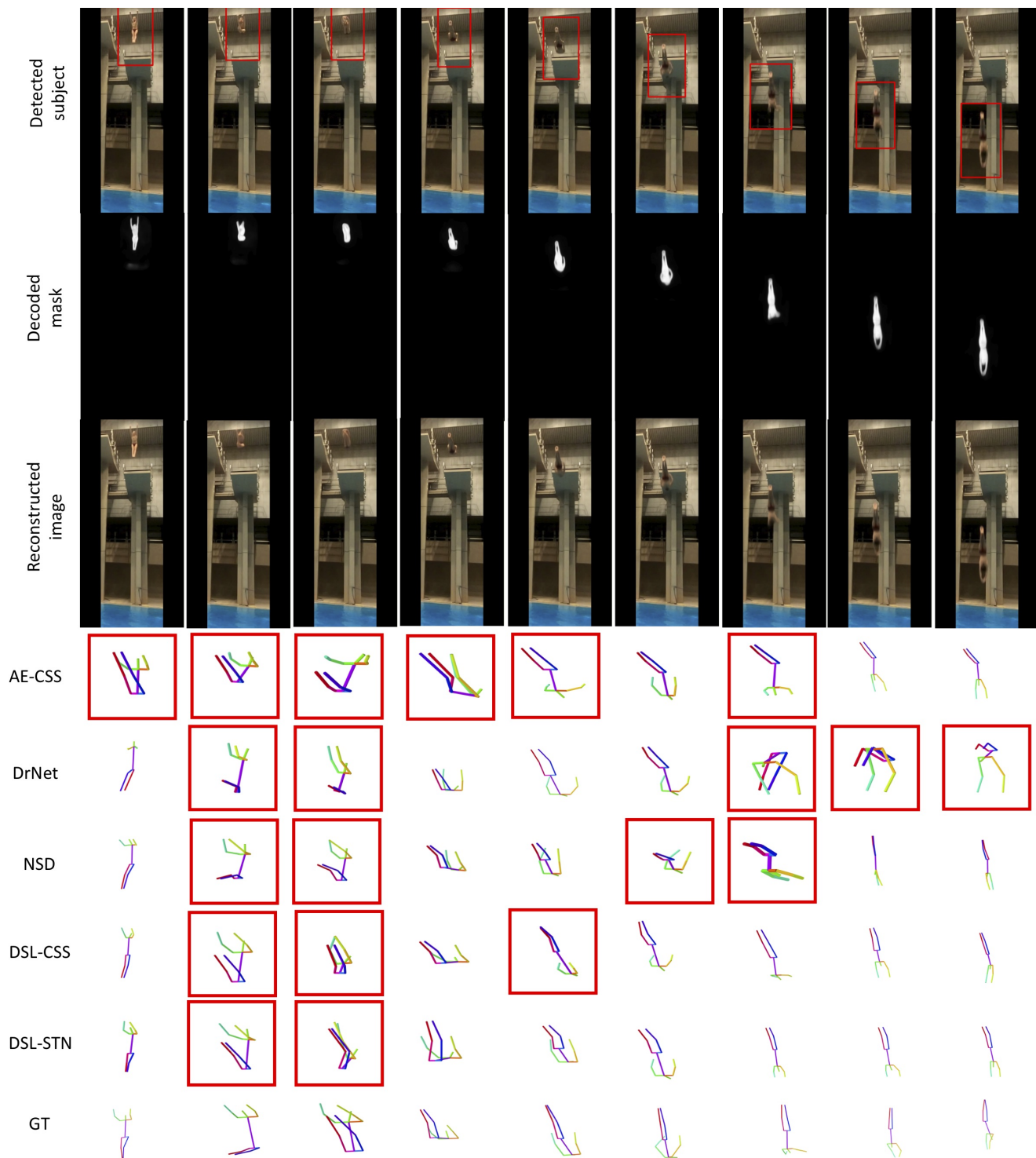


Figure S6. **Qualitative results on Diving Dataset.** Samples are taken from the test set. In the top row, the red rectangle shows the bounding box detected by our model for image cropping. The second and third rows, show respectively the decoded mask and image. Bottom rows, show the pose estimation by different models, where the red rectangle indicates pose estimation with a high error. GT in the bottom row indicates the ground truth labels.

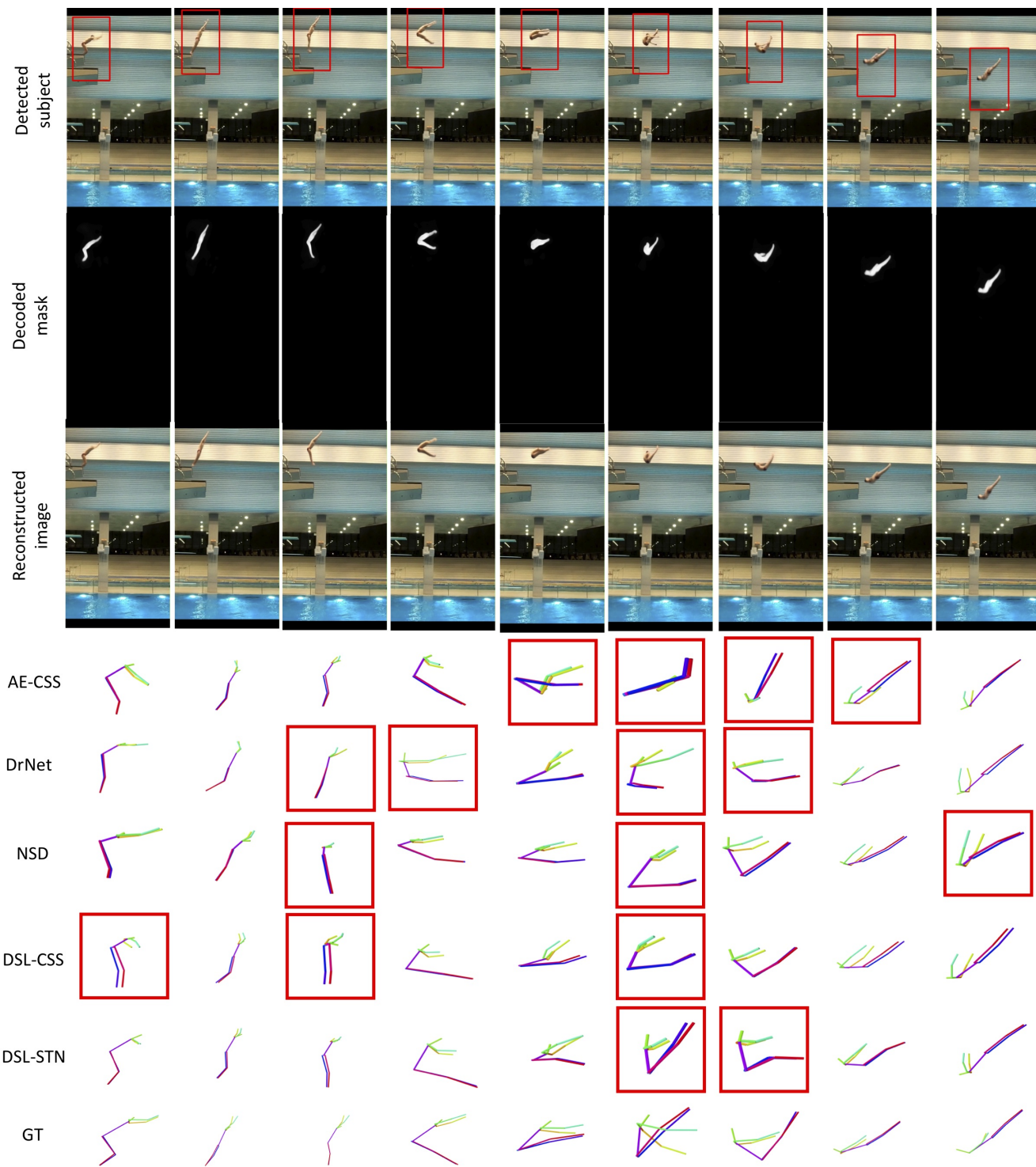


Figure S7. **Qualitative results on Diving Dataset.** Samples are taken from the test set. In the top row, the red rectangle shows the bounding box detected by our model for image cropping. The second and third rows, show respectively the decoded mask and image. Bottom rows, show the pose estimation by different models, where the red rectangle indicates pose estimation with a high error. GT in the bottom row indicates the ground truth labels.